



# Enhanced dry reforming of CO<sub>2</sub> and CH<sub>4</sub> on photothermal catalyst Ru/SrTiO<sub>3</sub>

Ying Tang<sup>a</sup>, Yangyang Li<sup>a</sup>, Wentao Bao<sup>a</sup>, Wenxia Yan<sup>a</sup>, Jie Zhang<sup>a</sup>, Yifan Huang<sup>a</sup>, Han Li<sup>a</sup>, Zijun Wang<sup>a,b</sup>, Minmin Liu<sup>a,b</sup>, Feng Yu<sup>a,b,\*</sup>

<sup>a</sup> Key Laboratory for Green Processing of Chemical Engineering of Xinjiang Bingtuan, School of Chemistry and Chemical Engineering, Shihezi University, Shihezi 832003, China

<sup>b</sup> Carbon Neutralization and Environmental Catalytic Technology Laboratory, Bingtuan Industrial Technology Research Institute, Shihezi University, Shihezi 832003, China

## ARTICLE INFO

### Keywords:

Dry reforming of methane  
Photothermal catalysis  
Electron transfer  
DFT calculations  
Reaction mechanism

## ABSTRACT

CH<sub>4</sub> and CO<sub>2</sub>, which are greenhouse gases, can be converted into valuable syngas through the solar-powered photothermal dry reforming of methane (DRM); this process also facilitates the collection and storage of solar energy. However, conventional photothermal catalysts insufficient catalytic activity for light enhancement at high temperatures. Herein, we report a photothermal catalyst Ru/SrTiO<sub>3</sub>. The yields of CO and H<sub>2</sub> were 1.4–1.5 times those obtained using the thermocatalytic process at 600 °C and under 300-W xenon lamp irradiation. Based on in situ-irradiated X-ray photoelectron spectroscopy and density functional theory calculations, light can induce electron transfer from SrTiO<sub>3</sub> to Ru in Ru/SrTiO<sub>3</sub> catalysts and participate in CH<sub>4</sub> dehydrogenation and H<sub>2</sub> generation, lowering its reaction energy barrier. Moreover, photogenerated electrons can suppress the occurrence of inverse water–gas reaction. This study clarifies the mechanism of the photothermal DRM, providing a useful guide for the future solar photothermal conversion of greenhouse gases.

## 1. Introduction

Dry reforming of methane (DRM: CH<sub>4</sub> + CO<sub>2</sub> = 2CO + 2 H<sub>2</sub>) has attracted considerable research interest recently as it can help mitigate the adverse effects of global warming [1,2] and convert cheap carbon sources into fossil fuels [3,4]. Particularly, DRM, which can address both CH<sub>4</sub> and CO<sub>2</sub> [5], offers a promising pathway to achieve the carbon neutrality and carbon peaking goals. Additionally, DRM can generate an appropriate amount of syngas and convert them into high-value hydrocarbons using the Fischer–Tropsch process [6]. Therefore, the development of the DRM technology is of great importance in terms of carbon recycling. CH<sub>4</sub> and CO<sub>2</sub> are chemically stable (with C–H and C–O bond energies of ~430 and 750 kJ/mol, respectively) [7,8], and even with suitable catalysts, high reaction temperatures are usually required to obtain satisfactory yields [9–11]. However, the reaction temperatures in the range of 500–700 °C can cause rapid catalyst deactivation due to carbon deposition on the catalyst surface from side reactions, such as methane cracking [12]; when the reaction temperature is greater than 700 °C, high temperatures can cause the sintering of active components

on the catalyst [13], while hydrogen embrittlement can occur in the reactor [14]. In addition, higher fossil-fuel-based energy consumption and carbon emissions are observed at high temperatures. Therefore, researchers are working to achieve the conversion of CH<sub>4</sub> and CO<sub>2</sub> at low temperatures.

Recently, photothermal catalysis, which integrates photocatalytic and thermocatalytic techniques, has received increasing attention because it enables DRM reactions at low temperatures while exhibiting some unique and excellent properties. Li et al. [15]. reported a Pt/CeO<sub>2</sub> catalyst for the photothermal methane dry reforming reaction, which utilized Zn doping and MgO overlay to achieve H<sub>2</sub> and CO yields of more than nine and three times larger than those obtained through thermally driven DRM, respectively. Zhou et al. [16]. prepared Ni/Ga<sub>2</sub>O<sub>3</sub> light thermal catalysts using light to adjust the relationship between the two core competitive reactions in the stem reorganization of methane and increased the H<sub>2</sub>/CO ratio from 0.55 to 0.94. Xu et al. [17]. reported a Rh/Ce<sub>x</sub>WO<sub>3</sub> catalyst for photothermal DRM that can simultaneously invoke photothermal and photovoltaic processes, overcoming the thermodynamic limitations of DRM under conventional conditions and

\* Corresponding author at: Key Laboratory for Green Processing of Chemical Engineering of Xinjiang Bingtuan, School of Chemistry and Chemical Engineering, Shihezi University, Shihezi 832003, China.

E-mail address: [yufeng05@mail.ipc.ac.cn](mailto:yufeng05@mail.ipc.ac.cn) (F. Yu).

<https://doi.org/10.1016/j.apcatb.2023.123054>

Received 19 April 2023; Received in revised form 21 June 2023; Accepted 27 June 2023

Available online 29 June 2023

0926-3373/© 2023 Elsevier B.V. All rights reserved.

producing an excellent photochemical energy efficiency (LTCEE) of 4.65% at moderate light intensities. Despite the research progress in the dry reforming of photothermal methane [15–25], developing high-performance photothermally active catalysts is urgently needed and their mechanisms in different chemical environments must be explored.

Herein, we prepared a Ru/SrTiO<sub>3</sub> catalyst for photothermal DRM, which was found to have excellent catalytic activity and stability. The yields of H<sub>2</sub> and CO were 7.9–9.9 times those obtained using the thermocatalytic process at 350 °C and under 300-W xenon lamp irradiation. The yields of H<sub>2</sub> and CO during the photothermal process at 600 °C were 320.29 and 388.99 mmol·g<sup>-1</sup>·h<sup>-1</sup>, respectively, which were 1.4–1.5 times those obtained under pure thermal conditions. First, SrTiO<sub>3</sub> is one of the classical photocatalytic semiconductors with excellent thermodynamic stability and electron–hole separation, which has been proven to be a good carrier for photothermal DRM catalysts [26]. Second, Ru is one of the most widely used active components in thermocatalytic methane dry reforming [10,27,28], and in this study, it can effectively capture the photogenerated charge from SrTiO<sub>3</sub> to enhance the photothermal catalytic activity. Finally, *in situ*-irradiated X-ray photoelectron spectroscopic (XPS) with density functional theory calculations demonstrated that light-induced charge transfer can effectively promote CH<sub>4</sub> dehydrogenation with H<sub>2</sub> generation and reduce the occurrence of the inverse water–gas reaction, enhancing catalytic activity.

## 2. Experimental procedure

### 2.1. Catalyst preparation

RuCl<sub>3</sub>·xH<sub>2</sub>O (x = 3–5) and SrTiO<sub>3</sub> were purchased from Degussa and Maclean. Further, 1 wt% Ru/SrTiO<sub>3</sub> catalysts were prepared using the hydrothermal method. Then, 0.02 g RuCl<sub>3</sub>·xH<sub>2</sub>O was dissolved in 10 mL of deionized water and added to a hydrothermal kettle containing 1 g of dry carrier SrTiO<sub>3</sub> and 50 mL of deionized water. Then, they were hydrothermally heated at 180 °C for 24 h. The obtained suspension was filtered and washed to pH = 7 using deionized water and ethanol in turn. The solid powder was obtained, after drying at 80 °C for 8 h and full grinding, and this powder was reduced in hydrogen gas at a flow rate of 65 mL/min for 2 h at 500 °C to obtain the Ru/SrTiO<sub>3</sub> catalyst, and the metal Ru loading of Ru/SrTiO<sub>3</sub> was 0.29 wt% as measured using an inductively coupled plasma (ICP).

### 2.2. Catalyst characterization

X-ray diffraction (XRD) patterns were recorded using a Bruker D8 Advance with a Cu Kα source (λ = 0.154 nm). Scanning electron microscopic (SEM) images were captured using a Hitachi SU8020 scanning electron microscope. Transmission electron microscopy (TEM) and HRTEM images were captured by a TecnaiG2F30 system. Moreover, the elemental surface distributions (mappings) of various elements were obtained using an X-ray energy spectrometer (HORIBA EX-250). Ru loadings were determined using the ICP–optical emission spectrometry (ICP–OES) (Agilent 730). The chemical status and elemental composition of the photocatalysts were determined using an X-ray photoelectron spectrometer (Thermo Escalab 250Xi) with Al Kα radiation. *In situ*-irradiated XPS spectra were obtained using an electron spectrometer (PHI5000 Versaprobe III X-ray). The Raman spectra of the samples were tested on a Raman spectrometer (Renishaw inVia) (λ = 532 nm). Electron paramagnetic resonance (EPR) spectra were measured on a Bruker A300 spectrometer. Ultraviolet–visible (UV–Vis) diffuse reflectance spectra (UV–Vis DRS) were recorded on a Shimadzu UV-3600 spectrometer equipped with an integrating sphere (using BaSO<sub>4</sub> as the reflectance standard). Photoluminescence (PL) spectra were recorded on a photoluminescence spectrophotometer (FLS1000, UK) with a laser excitation wavelength of 365 nm. The electrochemical impedance spectroscopy and photocurrent density characterization of the samples

were performed on a CHI760E electrochemical workstation (CH Instruments, province, country).

### 2.3. Photothermal Dry Reforming of Methane

An atmospheric pressure-fixed bed reactor (PFD-5000) was used to evaluate the methane dry reforming performance of the catalyst. The reactor comprised a flat quartz tube with a length of 400 mm and inner diameter of 3 mm. The catalyst bed size in the middle of the quartz tube is 3 mm × 14 mm × 14 mm. An appropriate amount of quartz wool was filled from the bottom up, and 150 mg of catalyst mixed with an appropriate amount of quartz sand was filled in the catalyst bed to ensure uniform illumination and heating. The temperature of the catalyst bed was monitored using a k-type thermocouple inserted below the reactor. A 300-W xenon lamp (PLS-SXE300) was used as the light source, and the light was directed onto the catalyst in the quartz tube through the quartz window of the tube furnace. The catalytic reaction device diagram is shown in Fig. S1. To prevent Ru oxidation upon exposure to air, the Ru/SrTiO<sub>3</sub> catalyst samples were reheated under a 65 mL·min<sup>-1</sup> H<sub>2</sub> atmosphere for reduction to 500 °C for 2 h before being subjected to thermal and photothermal catalytic reactions. Then, the heating was stopped, and H<sub>2</sub> was replaced by N<sub>2</sub> until the temperature was reduced to 150 °C. Finally, the feed gas (CH<sub>4</sub>: CO<sub>2</sub>: N<sub>2</sub> = 36: 36: 28) was passed into the quartz reaction tube. The total flow was 45 mL·min<sup>-1</sup>, giving a gas hourly space velocity (GHSV) of 4592 h<sup>-1</sup>. The dry reforming performance of methane was tested at 0.1 MPa in the temperature range of 200–600 °C. The reacted gas was analyzed using a gas chromatograph (GC97Plus) equipped with a thermal conductivity detector and a flame ionization detector on a column-type TDX-01. During the performance test, water was discharged from the bottom of the reaction tube.

We calculated the H<sub>2</sub> yield, CO yield, and the ratio of H<sub>2</sub> to CO using the following equations:

$$Y_{H_2} = \frac{F \cdot \varphi_{in,N_2} \cdot \varphi_{out,H_2}}{\varphi_{out,N_2} \cdot m_{cat}}, \quad (1)$$

$$Y_{CO} = \frac{F \cdot \varphi_{in,N_2} \cdot \varphi_{out,CO}}{\varphi_{out,N_2} \cdot m_{cat}}, \quad (2)$$

$$R = Y_{H_2}/Y_{CO}, \quad (3)$$

where  $Y_{H_2}$  and  $Y_{CO}$  represent the yields of H<sub>2</sub> and CO, respectively,  $F$  represents the total molar flow rate of the feed gas,  $\varphi_{in,N_2}$  and  $\varphi_{in,N_2}$  represent the molar fractions of nitrogen in the feed gas and the outlet gas, respectively,  $\varphi_{out,H_2}$  and  $\varphi_{out,CO}$  represent the molar fractions of H<sub>2</sub> and CO in the outlet gas, respectively, and  $m_{cat}$  represents the mass of the catalyst.

According to Arrhenius formula the logarithm of the carbon dioxide reaction rate ( $\ln r_{CO_2}$ ) was plotted against the reciprocal of temperature ( $1/T$ ). and the activation energy ( $E_a$ ) was obtained from the slope.

$$r_{CO_2} = \frac{F_{in,CO_2} \cdot X_{CO_2}}{m_{cat}}, \quad (4)$$

$$\ln r_{CO_2} = \frac{E_a}{R} \left( -\frac{1}{T} \right) + \ln A, \quad (5)$$

Here,  $r_{CO_2}$  is the reaction rate of CO<sub>2</sub> (mol<sub>CO<sub>2</sub></sub>·g<sub>cat</sub>·s<sup>-1</sup>).  $F_{in,CO_2}$  is the flow rate of CO<sub>2</sub> intake air (mol<sub>CO<sub>2</sub></sub>·s<sup>-1</sup>),  $X_{CO_2}$  is the conversion rate of CO<sub>2</sub>.  $R$  is the molar gas constant (8.314 J·mol<sup>-1</sup>·K<sup>-1</sup>).  $A$  is the pre-factor,  $T$  is the thermodynamic temperature (K) of each temperature gradient.

### 2.4. Theoretical calculations

Spin-polarized DFT calculations were performed using the QuantumATK platform and the linear combination of orbitals correlation

function. For electron-ion interactions, the plane-wave pseudopotential in the projection augmentation (PAW) method was applied. The catalyst surface was simulated with  $(4 \times 5)$   $\text{SrTiO}_3$  (110) supercells and Ru single atoms (a total of 20 Sr, 20 Ti, 60 O, and 22 Ru atoms). The lattice parameters were  $a = 19.526 \text{ \AA}$ ,  $b = 11.046 \text{ \AA}$  and  $c = 15.523 \text{ \AA}$ . The  $\Gamma$ -centered k-point lattice in the Monkhorst-Pack scheme was used, which was set to  $(4 \times 4 \times 1)$  to monitor Brillouin sampling by energy convergence. In the climbing image driving the elastic band CI-NEB method calculation, the image was optimized until the force on the ion was less than  $0.02 \text{ eV/\AA}$ . The charge density difference was used to estimate the atomic charge. Further, the CI-NEB method was used to define the transition state analysis of the catalyst. The adsorption energy is defined as  $E_{\text{ads}} = E_{\text{total}} - E_{\text{slab}} - E_{\text{species}}$ , where  $E_{\text{total}}$ ,  $E_{\text{slab}}$ , and  $E_{\text{species}}$  are the energies of the whole system, the slab model, and reaction gas in vacuum, respectively.

### 3. Results and discussion

#### 3.1. Catalyst structure and morphology

Figs. 1(a) and 1(b) show the SEM images of  $\text{SrTiO}_3$  and  $\text{Ru/SrTiO}_3$  catalysts, respectively. These samples exhibit similar irregular bulk particle structures. It can be seen that the high temperature during the preparation and reduction of the catalyst did not have a significant effect on its structure. This may be due to the good thermal stability of  $\text{SrTiO}_3$ . BET characterization (Fig. S2, Table S1) show that  $\text{Ru/SrTiO}_3$  and  $\text{SrTiO}_3$  have very similar  $\text{N}_2$  adsorption-desorption isotherms, which are type IV isotherms with H3 hysteresis loops, indicating the presence of  $\text{SrTiO}_3$  nanoparticle aggregates. The physical properties such as specific surface area, pore capacity, pore size and pore size distribution are also very similar, and the loading of Ru did not affect the physical structure of  $\text{SrTiO}_3$  significantly.

The TEM image of the catalyst is shown in Fig. 1(c), where a large

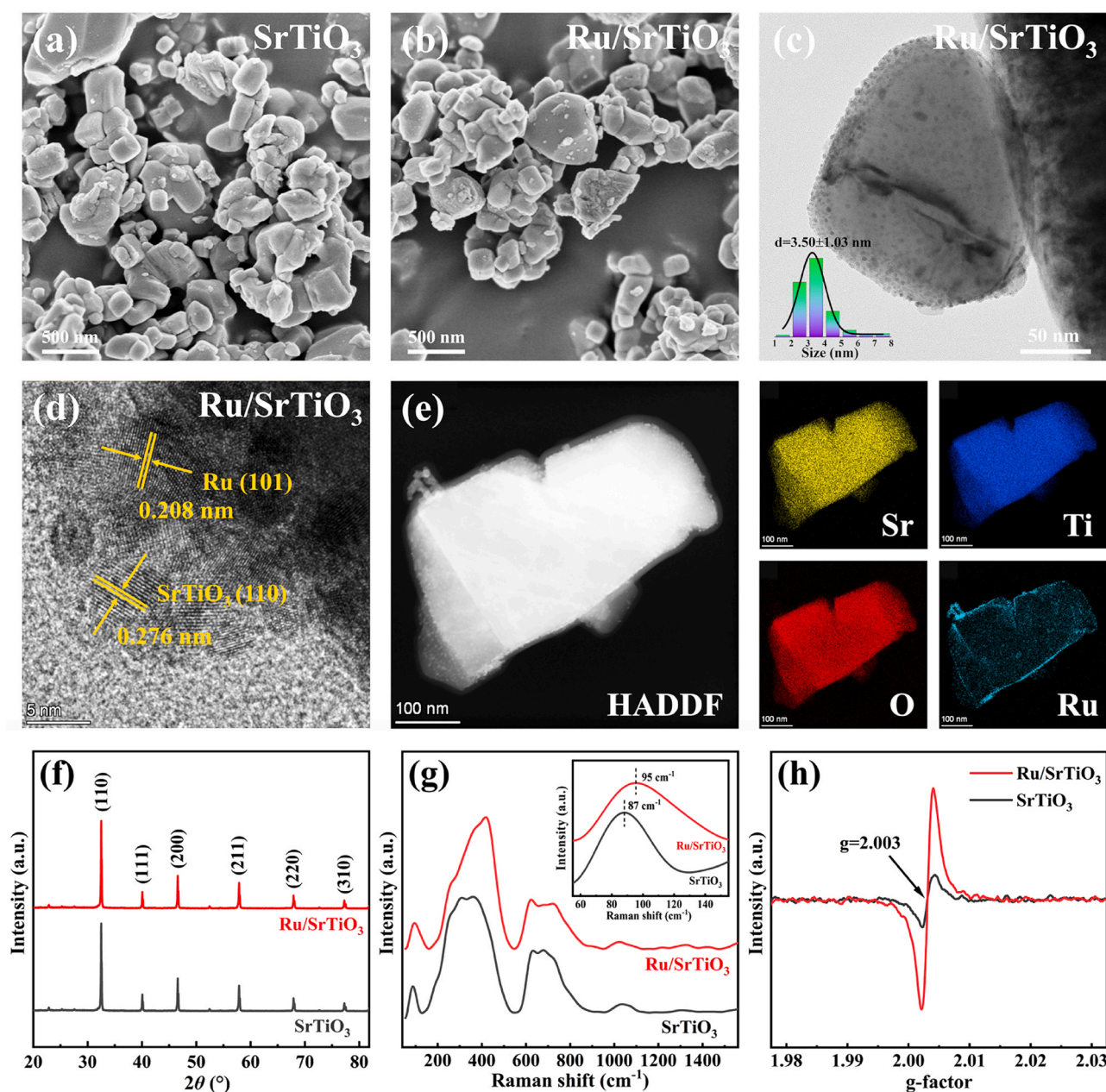


**Fig. 1.**  $\text{SrTiO}_3$  and  $\text{Ru/SrTiO}_3$  catalysts: (a-b) SEM images, (c) TEM images, (d) HRTEM images, (e) elemental distribution, (f) XRD spectra, (g) Raman spectra, (h) EPR.



number of small particles are uniformly distributed on the bulk carrier with particle sizes ranging from 1 to 8 nm and an average particle size of 3.5 nm. The HRTEM image shown in Fig. 1(d) proves that the small particles are metallic Ru, as the typical lattice spacing of 0.208 nm versus 0.276 nm on the crystal plane can be observed very clearly, which corresponds to the (101) crystal plane of metallic Ru and the (110) crystal plane of  $\text{SrTiO}_3$ , respectively. Fig. 1(e) shows the elemental distribution of the Ru/ $\text{SrTiO}_3$  sample. Ru species are uniformly distributed on the catalyst surface, providing a large number of active sites for the DRM reaction while enhancing the electron capture capability of Ru nanoparticles (NPs).

The structures of the catalysts were investigated via XRD, and the crystal structures of  $\text{SrTiO}_3$  and Ru/ $\text{SrTiO}_3$  catalysts were determined (Fig. 1f). The  $\text{SrTiO}_3$  crystal phase structure mainly contains (110), (111), (200), (211), (220), and (310) crystal planes. The XRD patterns of Ru/ $\text{SrTiO}_3$  and  $\text{SrTiO}_3$  are in complete agreement, and no characteristic diffraction peaks are observed with respect to Ru species, which is mainly attributed to the high dispersion and low loading of Ru NPs on  $\text{SrTiO}_3$  (ICP test results showed only 0.29 wt% Ru) [29]. Fig. 1(g) shows the Raman spectra of the Ru/ $\text{SrTiO}_3$  catalyst and carrier. Three large peaks can be observed in the wavenumber range of 0–2000  $\text{cm}^{-1}$ .

Among them, the peak at  $\sim 90 \text{ cm}^{-1}$  represents the TO1 mode of  $\text{SrTiO}_3$ , and two broad peaks exist in the range of 220–500 and 590–760  $\text{cm}^{-1}$ , which can be attributed to second-order Raman scattering [30,31]. The intensity of the Raman peak associated with the Ru/ $\text{SrTiO}_3$  catalyst was smaller than that associated with  $\text{SrTiO}_3$ , indicating the presence of defects on the surface or inside the Ru/ $\text{SrTiO}_3$  catalyst. Moreover, owing to the presence of oxygen vacancies or lattice defects in  $\text{SrTiO}_3$  NPs, we observed that the Raman peaks of Ru/ $\text{SrTiO}_3$  shifted to the high-wavenumber side compared to those of  $\text{SrTiO}_3$  [32]. Hence, we can conclude that the loading of Ru NPs increases the concentration of oxygen vacancies or lattice defects in  $\text{SrTiO}_3$ .

To further identify oxygen vacancies, EPR spectroscopy was performed, as shown in Fig. 1(h). A pair of sharp symmetric peaks at  $g = 2.003$  indicates that electrons are captured at defect sites, indicating the presence of oxygen vacancies, while the EPR signal is more pronounced for the Ru-loaded catalyst, indicating more oxygen vacancies. The performance of metal oxide catalysts benefits from the presence of oxygen vacancies. On the one hand, the presence of oxygen vacancies can shift the oxide Fermi energy level upward, resulting in defective energy levels in the bandgap. This reduces the energy bandwidth and improves the light absorption performance. On the other hand, oxygen

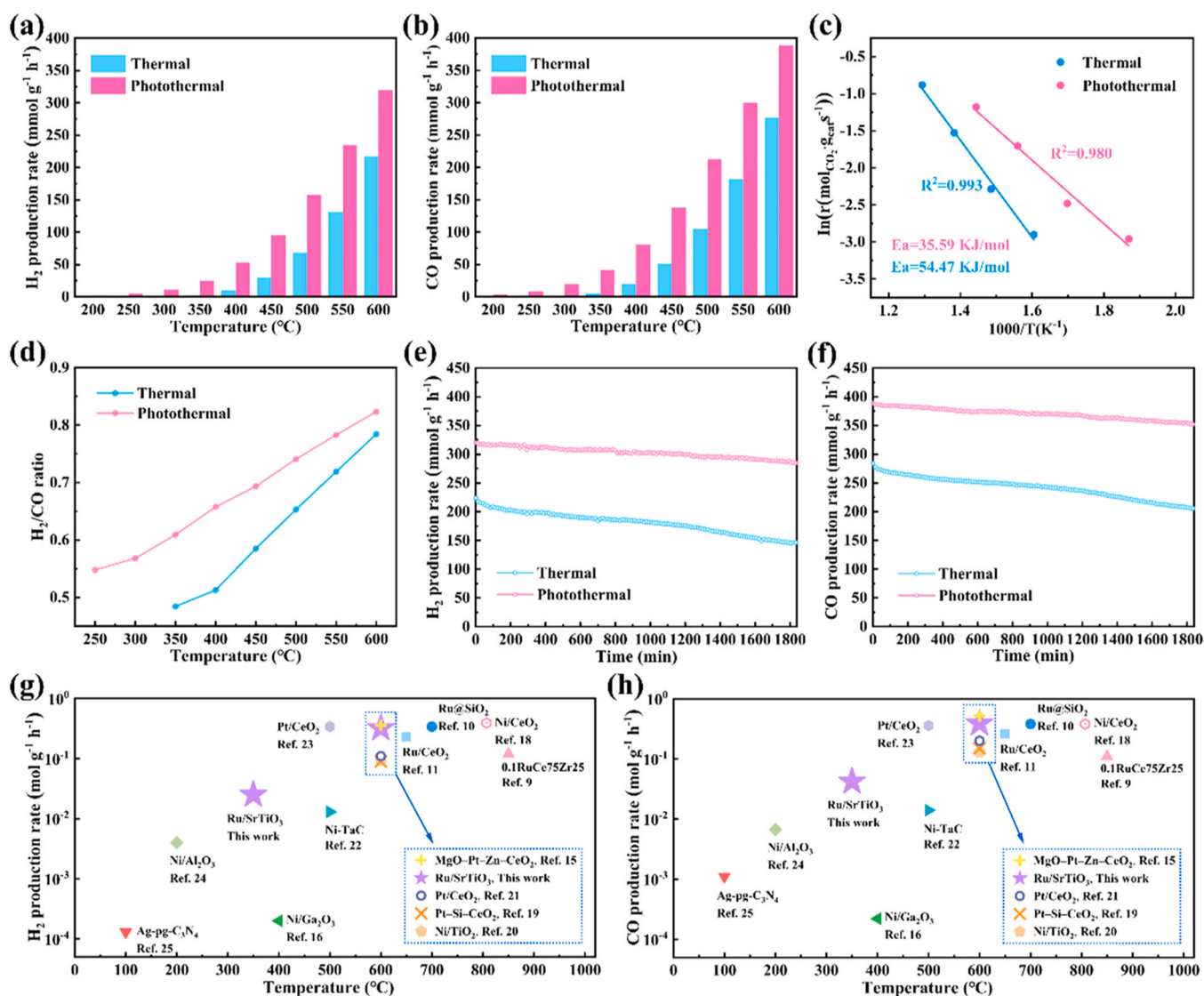


Fig. 2. Methane dry reforming activity of Ru/ $\text{SrTiO}_3$  catalysts under photothermal and thermal catalytic processes: (a) yield of  $\text{H}_2$ , (b) yield of CO, (c) Arrhenius curve, (d) the  $\text{H}_2/\text{CO}$  ratio, (e–f) yield in 1800 min stability test and (g–h) Comparisons of yields of  $\text{H}_2/\text{CO}$  of Ru/ $\text{SrTiO}_3$  photothermal catalyst with the results in literatures.



vacancies have been shown to be important for methane dry reforming reactions, where methane is usually decomposed on metals and carbon dioxide is activated on oxygen vacancies [33,34]. Therefore, the presence of oxygen vacancies may help in improving the catalytic performance of Ru/SrTiO<sub>3</sub> materials.

### 3.2. Performance of catalysts

The catalytic activity of the catalysts under the photothermal (PT) and thermal (T) processes was evaluated by testing the methane dry reforming performance of the catalysts in the temperature range of 200–600 °C, as shown in Fig. 2. Because commercial SrTiO<sub>3</sub> has no methane dry reforming activity in PT and T processes at any temperature, it is not marked in the figure.

Figs. 2(a) and 2(b) show the yields of H<sub>2</sub> and CO at different temperatures for different processes. In the T process, the Ru/SrTiO<sub>3</sub> catalyst produced H<sub>2</sub> and CO only at 350 °C with yields of 2.57 and 5.30 mmol·g<sup>-1</sup>·h<sup>-1</sup>, respectively, whereas in the PT process, the products were already produced at 200 °C (the minimum temperature for product generation dropped by 150 °C), and the yields of H<sub>2</sub> and CO were 2.10 and 3.57 mmol·g<sup>-1</sup>·h<sup>-1</sup>, respectively. The yields of H<sub>2</sub> and CO in the PT process reached 25.43 and 41.76 mmol·g<sup>-1</sup>·h<sup>-1</sup> at 350 °C, which were 9.9 and 7.9 times those obtained using the T process at the same temperature. The higher yields under illumination confirm that the photocatalytic process contributes to reducing the activation reaction temperatures of CO<sub>2</sub> and CH<sub>4</sub> and increasing the syngas yields.

The product yields of the PT and T processes increased considerably with increasing temperature; however, the difference between them gradually decreased because DRM is a strong heat-absorbing reaction and high temperature is beneficial to the reaction, which exerts a greater influence on the reaction, gradually diminishing the effect of light on the reaction. However, even when the temperature increased to 600 °C, the yields of H<sub>2</sub> and CO under the PT process were 320.29 and 388.99 mmol·g<sup>-1</sup>·h<sup>-1</sup>, respectively, which were 1.5 and 1.4 times those obtained via the T process, indicating that light promotes the reaction at high temperatures.

Light does significantly enhance the yield of the product for two possible reasons. First, light causes an increase in temperature, which enhances the catalytic activity. Second, the photogenerated charge is involved in the reaction, lowering the energy barrier of the reaction and thus enhancing the catalytic activity.

The xenon lamp light source is equipped with a cold reflector and can output light in the wavelength range of 320–780 nm. During the photothermal experiments, it does not output NIR-IR light with strong thermal effects. However, it was found that temperature differences did exist in the catalyst bed under light and non-light conditions, as shown in Table S2. The temperature difference is about 10 °C, and this temperature difference does not have a large effect on the catalytic activity. This is because the catalytic activity at 550 °C under photothermal conditions is also higher than that at 600 °C under thermal conditions.

However, in order to verify the possibility of light increasing temperature and enhancing reaction activity, two experiments were conducted. First, ruthenium metal particles were loaded on Al<sub>2</sub>O<sub>3</sub> by the same preparation method, and the properties were tested under photothermal and thermal conditions, respectively. As Al<sub>2</sub>O<sub>3</sub> is not a photocatalytic material, the performance enhancement on it can be attributed entirely to the temperature increase caused by light. The test results are shown in Fig. S3. The results proved that the activity of Ru/Al<sub>2</sub>O<sub>3</sub> catalyst is much less than Ru/SrTiO<sub>3</sub> catalyst, but the light can increase the temperature and has a large effect on the catalytic activity. It was found that the activity enhancement was increasing with the increase of temperature. Under the photothermal condition at 600 °C, the yield of H<sub>2</sub> and CO was enhanced by 41% and 36%, respectively, compared to the thermal condition. This may be due to the continuous heat accumulation of the catalyst by light.

Since the temperature increase caused by light will significantly

increase the activity, is this the only reason for the performance improvement of Ru/SrTiO<sub>3</sub> catalyst under light? To investigate it, the catalytic activity of Ru/SrTiO<sub>3</sub> was tested in UV (320–400 nm), and visible light (400–780 nm) with two filters, respectively. The UV filter is PLS-LF02 liquid filter, which can greatly reduce the thermal effect of light on photocatalytic reaction. Xenon lamps equipped with this filter can be considered as cold light sources. The use of visible light filters, on the other hand, still has some thermal impact on the system.

The performance test results are shown in Fig. S4. The results show that the catalytic activity of Ru/SrTiO<sub>3</sub> under visible light was increased, which is mainly due to the increase in temperature caused by light. The largest enhancement of reaction activity was observed under UV light irradiation. This indicates that UV irradiation on the catalyst surface can induce electron transfer from SrTiO<sub>3</sub> carriers to Ru and can greatly enhance the catalytic activity of the reaction. These results indicated that the higher temperature generated by light and the light-induced charge transfer are the two reasons for the enhanced catalytic performance under light. And, the light-induced charge transfer plays a more critical role in the light-driven DRM.

To examine the reaction mechanism in the PT and T processes, the kinetic analysis of the dry reforming reaction of methane over the Ru/SrTiO<sub>3</sub> catalyst was performed, as shown in Fig. 2(c). The natural log ln (K) was plotted against the inverse of the absolute temperature (1/T) by the Arrhenius equation, and apparent activation energy values (E<sub>a</sub>) with different slopes were obtained via linear fitting [35]. The E<sub>a</sub> of the dry reforming reaction of methane under the PT process (35.59 kJ/mol) was lower than that under the T process (54.47 kJ/mol), indicating that the addition of light significantly reduces the kinetic barriers of the Ru/SrTiO<sub>3</sub>-catalyzed methane dry reforming reaction, which is favorable for the reaction to proceed.

Further, the CO yield was greater than the H<sub>2</sub> yield for the PT and T processes. To observe this phenomenon more clearly, the ratio of H<sub>2</sub> to CO yields at different temperatures was plotted, as shown in Fig. 2(d). In this experiment, the reaction stoichiometry ratio of CO<sub>2</sub> and CH<sub>4</sub> was 1:1, and equal amounts of CO and H<sub>2</sub> were produced because we did not observe other products. The higher CO yields may be due to the occurrence of the reverse water–gas shift (RWGS) reaction, which refers to the reaction of CO<sub>2</sub> with H<sub>2</sub> to form CO and H<sub>2</sub>O (CO<sub>2</sub> + H<sub>2</sub> = CO + H<sub>2</sub>O) and is widely used in DRM. It is the most significant side reaction of DRM [16] because it consumes H<sub>2</sub> and produces CO and therefore results in a H<sub>2</sub> yield lower than that of CO. As can be observed in Fig. 2 (d), the ratio of H<sub>2</sub> to CO increases with increasing temperature, while the ratio of H<sub>2</sub> to CO is higher for the PT process than that for the T process at any temperature. The higher H<sub>2</sub> to CO ratios suggest that the introduction of light contributes to the higher H<sub>2</sub> ratios because either light contributes to H<sub>2</sub> production or the introduction of light reduces the occurrence of the RWGS reaction, which will be further discussed in the subsequent characterization.

In addition to the significant enhancement of DRM activity under light, catalytic stability is an important issue as it determines the long-term usability of the catalysts. We further investigated the effect of light on the stability of DRM and measured its stability in the dark as a reference, with a test temperature of 600 °C and a test time of ≥ 1800 min. As shown in Figs. 2(e) and 2(f), after 1800 min of testing, the yield of H<sub>2</sub> in the PT process decreased from the initial 320.29–289.25 mmol·g<sup>-1</sup>·h<sup>-1</sup> (a decrease of 9.7%), while the yield of H<sub>2</sub> in the T process decreased from 217.54 to 148.84 mmol·g<sup>-1</sup>·h<sup>-1</sup> (a decrease of 31.6%). Similarly, the CO yields in the PT and T processes decreased by 8.6% and 24.3%, respectively. The catalyst decay was significantly reduced after the introduction of light, implying that light not only enhances the methane dry reforming activity but also improves the durability of the thermocatalytic methane dry reforming reaction. It is worth noting that the catalyst activity decreases rapidly during thermal catalysis, which means that the increase in temperature generated by light is detrimental to the stability of the catalyst. In fact, light maintains the stability of the catalyst, and it is highly likely that

photogenerated charges play an important role in this. This will be discussed in a later section.

The stability of CH<sub>4</sub> and CO<sub>2</sub> conversions (Fig. S5) show that the initial conversion of CH<sub>4</sub> at 600 °C are 58% and 43% for the photo-thermal and thermal processes, respectively. And the conversions of CO<sub>2</sub> are 71% and 55%, respectively. The DRM reaction is a strong heat absorption reaction, and thermocatalytic DRM usually requires high temperatures of 700–1000 °C. Thus, the conversion obtained at 600 °C under photothermal conditions has reached a good level.

To better understand the catalytic ability of Ru/SrTiO<sub>3</sub> catalysts, Fig. 2(g)–(h) and Table 1 list the current status of research on DRM catalysts in recent years. Simply comparing conversion rates is not accurate because of the various space velocities used in different reports. To facilitate the comparison, the yields of the catalysts were calculated based on the parameters given in the literature. The results in Fig. 2(g)–(h) and Table 1 show that the Ru/SrTiO<sub>3</sub> catalysts possess good catalytic activity and are comparable and even superior to the recently reported catalysts.

### 3.3. Optical and optoelectronic properties

In order to investigate the optical and electronic properties of the samples and to explore the role played by photogenerated charges in the reaction. A series of optical and optoelectronic properties of the catalyst were characterized. This is shown in Fig. 3. First, we examined the UV–Vis spectra of the SrTiO<sub>3</sub> and Ru/SrTiO<sub>3</sub> catalysts in the range of 200–800 nm (Fig. 3(a)). Both samples exhibited significant light absorption in the UV band ranging from 200 to 400 nm, indicating that the samples possess good UV adsorption ability, which can be attributed to the presence of SrTiO<sub>3</sub>. In the visible region, the absorption intensity of the Ru/SrTiO<sub>3</sub> catalyst was higher than that of pure SrTiO<sub>3</sub>, implying that Ru/SrTiO<sub>3</sub> has better visible-light absorption than SrTiO<sub>3</sub>. Meanwhile, in the spectral range of 200–800 nm, the light absorption ability of Ru/SrTiO<sub>3</sub> was better than that of SrTiO<sub>3</sub>, indicating that the catalyst has good light absorption ability. The addition of Ru to SrTiO<sub>3</sub> can form a heterogeneous structure and broaden the optical response range of the Ru/SrTiO<sub>3</sub> catalyst, thereby obtaining a better catalytic activity for DRM compared to conventional thermal catalysts [20].

The PL emission spectra of the prepared catalysts were examined to evaluate the recombination behavior of electrons and holes generated via photoexcitation in the semiconductor, as shown in Fig. 3(b). Because the photoluminescence mainly originated from the recombination of photogenerated carriers with holes, the weaker photoluminescence intensity indicates the low density of the recombination center. In the wavelength range of 400–600 nm, the intensity of the emission peak of Ru/SrTiO<sub>3</sub> was significantly lower than that of SrTiO<sub>3</sub>, indicating that the photoexcitation of Ru/SrTiO<sub>3</sub> samples produces less efficient electron–hole recombination. This is attributed to the formation of a Ru-

SrTiO<sub>3</sub> heterostructure, where Ru can effectively trap the excited electrons in the valence layer of SrTiO<sub>3</sub> so that the electrons are effectively separated from the holes and participate in the redox reactions occurring on the catalyst surface, thereby improving the photocatalytic activity of the catalyst.

To further verify the separation effect of photoexcited electron–hole pairs, we performed transient photocurrent response tests under intermittent xenon lamp illumination, as shown in Fig. 3(c). After several cycles of testing, the results showed that both samples have good reproducibility, and the significantly higher photocurrent density of Ru/SrTiO<sub>3</sub> indicates that the photogenerated carriers are effectively separated and more electrons and holes participate in the redox process, resulting in the improved photocatalytic activity of the catalyst [36,37], which is consistent with the photoluminescence spectroscopy results.

To further confirm this conclusion, electrochemical impedance tests of SrTiO<sub>3</sub> and Ru/SrTiO<sub>3</sub> were conducted in the absence and presence of light, as shown in Fig. 3(d). It is known that a decrease in the radius of the Nyquist curve arc represents a decrease in the carrier transfer resistance of the semiconductor and higher transmission efficiency [38]. The arc radii of both samples under light were smaller than those measured in the dark. Particularly, Ru/SrTiO<sub>3</sub> showed the smallest arc radius under visible-light irradiation, indicating that Ru/SrTiO<sub>3</sub> is more favorable for charge separation and transport under illumination.

*In situ*-irradiated XPS was used to explore the charge transfer between SrTiO<sub>3</sub> and Ru. As shown in Fig. 4, the elemental composition of the sample involved Sr, Ti, O, and Ru. The C 1 s peak of the sample was calibrated to 284.8 eV. The peak positions and the amount of change in the electronic configuration of each element are recorded in Table S3. The high-resolution Sr 3d spectrum of the Ru/SrTiO<sub>3</sub> catalyst is shown in Fig. 4(a), indicating the symmetric Sr 3d double peaks of Sr<sup>2+</sup> with binding energies of 133.3 and 135.1 eV, respectively, in the dark environment, whereas in the presence of light, their binding energies shifted to 133.5 and 135.3 eV, respectively (the Sr 3d peak shifted by 0.2 eV).

The lattice oxygen (O<sub>L</sub>) and OH surface groups (O<sub>OH</sub>) in Fig. 4(b), both positively shifted the binding energy by 0.3 eV under light. In Fig. 4(c), light shifted the binding energy of Ti 2p<sub>1/2</sub> and Ti 2p<sub>3/2</sub> positively by 0.2 eV. At the same time, the binding energy of Ru 3p<sub>3/2</sub> peak negatively shifted by 0.3 eV. Ru 3d<sub>3/2</sub> in Fig. 4(d) is similarly negatively shifted by 0.2 eV.

In conclusion, light shifts the binding energies of Sr, Ti, and O positively and that of Ru negatively, meaning that the electron density of SrTiO<sub>3</sub> decreases while that of Ru increases under light exposure. This indicates that the photogenerated electrons in the conduction band of photoexcited SrTiO<sub>3</sub> can be transferred to the adjacent Ru NPs [39]. On the one hand, during the transfer of electrons from SrTiO<sub>3</sub> NPs with higher Fermi energy to the surface of Ru NPs, the SrTiO<sub>3</sub> valence band bends upward until both Fermi energy levels reach the same level [40]. In this process, the Schottky barrier is formed at the interface of Ru and

**Table 1**  
Summary of methane dry reforming catalyst performance.

Catalysts	Reaction process	T (°C)	H <sub>2</sub> production rate (mol·g <sup>-1</sup> ·h <sup>-1</sup> )	CO production rate (mol·g <sup>-1</sup> ·h <sup>-1</sup> )	Ref.
0.1RuCe75Zr25	Thermal	850	1.2 × 10 <sup>-1</sup>	1.1 × 10 <sup>-1</sup>	[9]
Ru@SiO <sub>2</sub>	Thermal	700	3.4 × 10 <sup>-1</sup>	3.8 × 10 <sup>-1</sup>	[10]
Ru/CeO <sub>2</sub>	Thermal	650	2.3 × 10 <sup>-1</sup>	2.6 × 10 <sup>-1</sup>	[11]
Ni/CeO <sub>2</sub>	Photothermal	807	3.9 × 10 <sup>-1</sup>	3.8 × 10 <sup>-1</sup>	[18]
Pt–Si–CeO <sub>2</sub>	Photothermal	600	9.0 × 10 <sup>-2</sup>	1.5 × 10 <sup>-1</sup>	[19]
Ni/TiO <sub>2</sub>	Photothermal	600	9.2 × 10 <sup>-2</sup>	1.3 × 10 <sup>-1</sup>	[20]
Pt/CeO <sub>2</sub>	Photothermal	600	1.1 × 10 <sup>-1</sup>	2.0 × 10 <sup>-1</sup>	[21]
Ru/SrTiO <sub>3</sub>	Photothermal	600	3.2 × 10 <sup>-1</sup>	3.9 × 10 <sup>-1</sup>	This work
MgO–Pt–Zn–CeO <sub>2</sub>	Photothermal	600	3.6 × 10 <sup>-1</sup>	5.2 × 10 <sup>-1</sup>	[15]
Ni–TaC	Photothermal	500	1.3 × 10 <sup>-2</sup>	1.4 × 10 <sup>-2</sup>	[22]
Pt–CeO <sub>2</sub>	Photothermal	500	3.4 × 10 <sup>-1</sup>	3.6 × 10 <sup>-1</sup>	[23]
Ni/Ga <sub>2</sub> O <sub>3</sub>	Photothermal	400	2.0 × 10 <sup>-4</sup>	2.2 × 10 <sup>-4</sup>	[16]
Ru/SrTiO <sub>3</sub>	Photothermal	350	2.5 × 10 <sup>-2</sup>	4.2 × 10 <sup>-2</sup>	This work
Ni–Al <sub>2</sub> O <sub>3</sub>	Photothermal	200	4.0 × 10 <sup>-3</sup>	6.7 × 10 <sup>-3</sup>	[24]
Ag–pg-C <sub>3</sub> N <sub>4</sub>	Photothermal	100	1.3 × 10 <sup>-4</sup>	1.1 × 10 <sup>-3</sup>	[25]

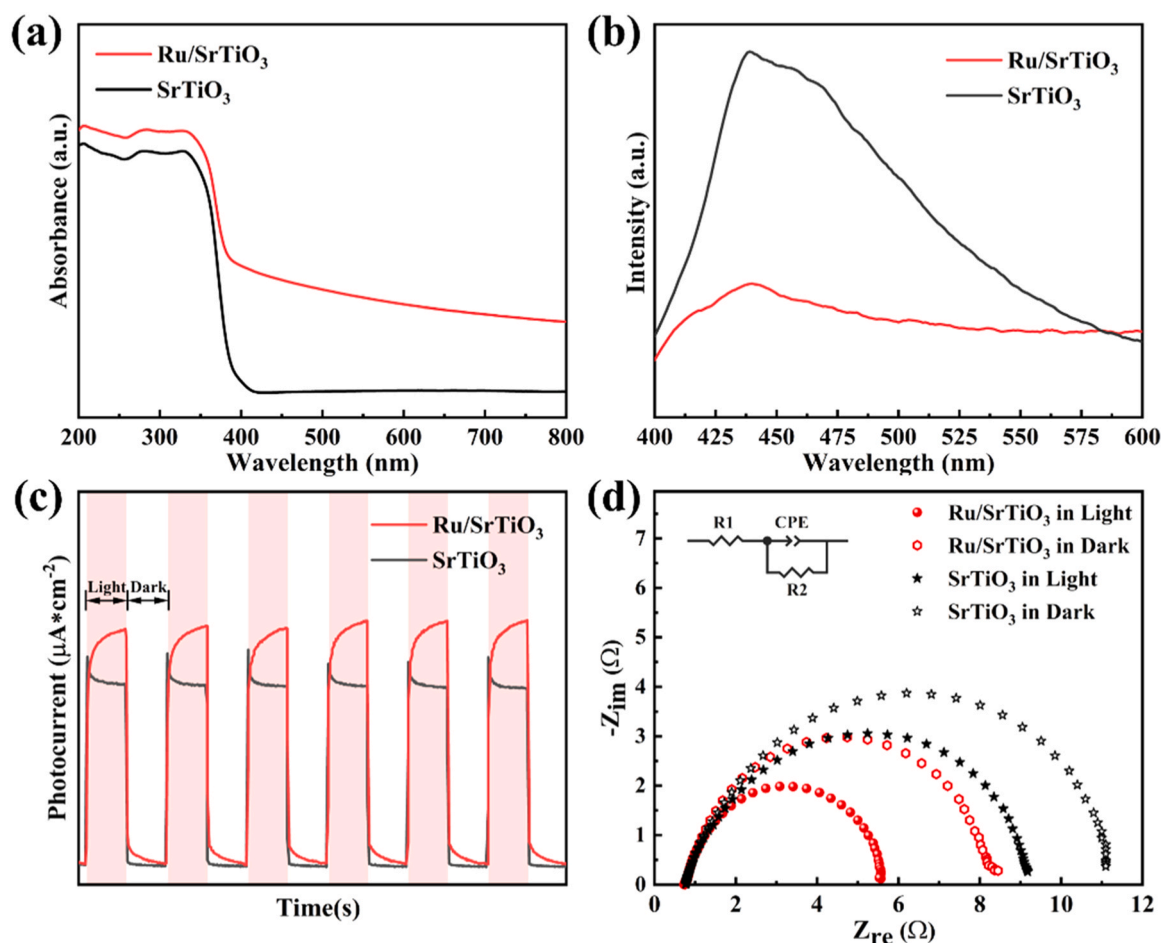


Fig. 3. SrTiO<sub>3</sub> and Ru/SrTiO<sub>3</sub> catalysts: (a) UV-Vis spectra, (b) photoluminescence spectra, (c) transient photocurrent response with (d) impedance plots.

SrTiO<sub>3</sub>, which can effectively trap electrons, reduce the recombination of photogenerated electrons and holes, and improve photocatalytic activity. On the other hand, in the DRM reaction, Ru<sup>0</sup> is the active center of the reaction. Electrons accumulated in Ru NPs can maintain the reduced state of Ru, and these electrons can participate in the DRM reaction by band-to-band leap and promote the reaction. This may be another reason for the catalytic activity enhancement by light.

To determine changes in Ru during the reaction, the Ru/SrTiO<sub>3</sub> catalyst after 8 h of thermal reaction and the catalyst after 8 h of photothermal reaction were characterized through XPS, as shown in Fig. 4 (e). By analyzing and processing the peak area of Ru 3d<sub>3/2</sub>, we observed that the percentage of Ru<sup>0</sup> was 53% after the pure thermal reaction; however, after the photothermal reaction, the percentage of Ru<sup>0</sup> increased to 60%. This is consistent with the conclusion obtained from the in situ-irradiated XPS results, which states that the electrons are transferred from SrTiO<sub>3</sub> to Ru under light conditions and that these electrons help to maintain the reduced state of Ru in the catalyst, maintaining the proportion of Ru<sup>0</sup> in the active site [41]. This leads to more stable catalyst activity under light conditions.

DFT calculations were used to explore the catalyst properties under light and dark conditions as well as the step diagram of the reaction. *In situ*-irradiation XPS spectroscopy has demonstrated that photogenerated electrons are injected into Ru; Therefore, electrons were enriched artificially on Ru and an electron-rich condition was created in the system using this method to simulate light. [16,42,43]. It is worth noting that electrons are artificially added to Ru, but it cannot be determined whether the electrons will eventually be enriched on Ru because the charge will be redistributed among nearby atoms. Therefore, the actual transferred electrons need to be calculated by Bader charge analysis. An

excessive number of Ru atoms can complicate the energy band structure and density of states, and it is difficult to obtain valuable information from them. Therefore, in order to qualitatively discuss the energy band structure and density of states, in this section, a simple model is built containing only the SrTiO<sub>3</sub> model and a single Ru atom with added an electron. As the whole system is in charge conservation and enriched with electrons on Ru atoms, the corresponding holes appear automatically in SrTiO<sub>3</sub>.

Electron transfer and distribution were initially calculated to verify the successful enrichment of electrons on Ru. The Ru/SrTiO<sub>3</sub> charge density and Bader charge analysis are shown in Figs. 4(f) and 4(g). Compared to the dark reaction, electrons around the metal Ru under illumination conditions accumulate more on the catalyst surface, remarkably increasing the charge density of Ru. In the absence of light, the electrons of Ru on the catalyst decreased by 0.26 e, whereas under light conditions, the electrons on Ru increased by 0.18 e. A partial charge transfer of electrons from SrTiO<sub>3</sub> to Ru occurs. The Bader charge analysis can show that the simulated light method used is consistent with the in situ XPS characterization results, which provides the basis for the next DFT calculations.

According to the “accept–donate” principle, Ru in Ru/SrTiO<sub>3</sub> has a 4d<sup>8</sup> configuration; thus, the empty d orbitals of Ru atoms can accept electrons generated by the photoexcitation of SrTiO<sub>3</sub> [44–46]. Thus, the Ru still adds a partial charge after the charge is redistributed among the nearby atoms.

Next, this model was used to calculate the effective electronic band structure of Ru/SrTiO<sub>3</sub> catalyst in the absence and presence of light, and the results are shown in Figs. 5(a) and 5(b). In the absence of light, the valence band (VB) of Ru/SrTiO<sub>3</sub> is full of electrons and its conduction



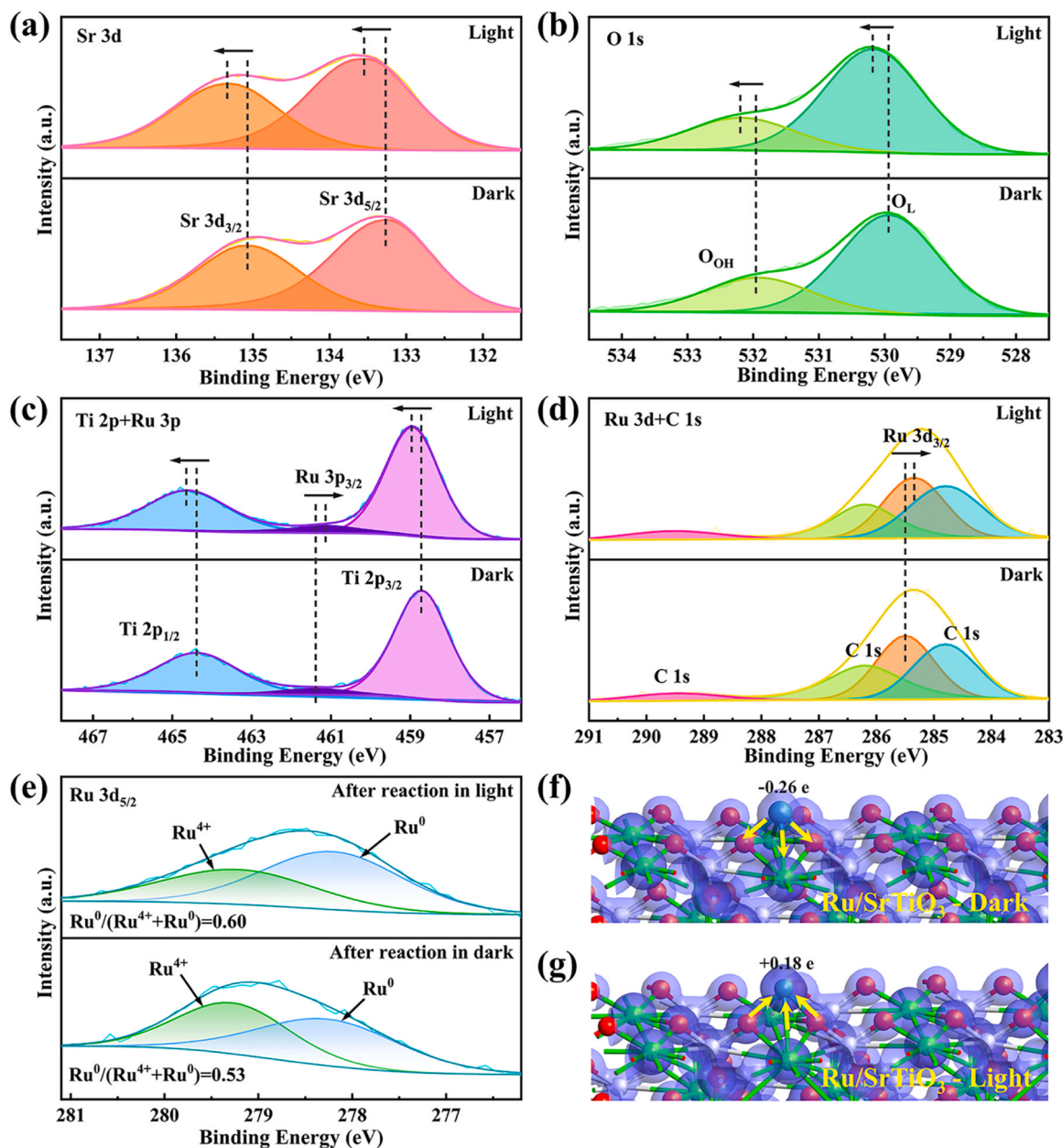


**Fig. 4.** *In situ*-irradiated XPS spectra of Ru/SrTiO<sub>3</sub> catalysts: (a) Sr 3d, (b) O 1s, (c) Ti 2p and Ru 3p, and (d) Ru 3d and C 1s (e) XPS spectra of Ru 3d<sub>5/2</sub> of Ru/SrTiO<sub>3</sub> catalysts after the reaction (dark reaction at 600 °C for 8 h; light reaction at 600 °C for 8 h). (f, g) Charge density differences.

band (CB) is all empty orbitals. After illumination, the electron orbitals on the VB move to the vicinity of the Fermi energy level, indicating that the electrons inside the catalyst, after gaining enough energy, can easily break away from the valence bond and get excited from the VB to the CB and participate in the subsequent photocatalytic reaction.

Projected density of states (PDOS) can further decode important information regarding the electronic structure properties of metal/semiconductor complexes. Therefore, we selected the main orbitals of each element and plotted the Ru/SrTiO<sub>3</sub> PDOS in the absence and presence of light, as shown in Figs. 5(c) and 5(d). Ru/SrTiO<sub>3</sub> mainly comprised Sr 3d, Ti 3d, Ru 3d, and O 2p orbitals, which were distributed on both sides of the Fermi energy level. In the absence of light, the bottom of the CB mainly comprised Ti 3d orbitals and the top of the VB mainly involved O 2p orbitals. Meanwhile, extremely close Ru 3d orbitals existed on the left side of the Fermi energy level with a large gap between them and O 2p orbitals. In the presence of light, the bottom-most part of the CB involved Ru 3d orbitals. The hybridization between

O 2p, Ti 3d, and Ru 3d orbitals at the top of the VB increased and became closer to the Fermi energy level. These results showed that the introduction of light promotes interactions between Ru and SrTiO<sub>3</sub> and facilitates the induction of electron transfer from SrTiO<sub>3</sub> to Ru, which increases the electron density of Ru NPs and thus enhances the activity of photoassisted CO<sub>2</sub> methane reforming. These observations are consistent with the previous findings.

#### 3.4. Reaction mechanism

For the DRM reaction, it is widely accepted that the dissociation of the C–H bond in the CH<sub>4</sub> molecule is the limiting step [47] because once the first H of the CH<sub>4</sub> molecule is dissociated, the other H is removed rapidly, and eventually, C is generated. The deposited carbon combines with oxygen atoms to form CO, and the generated H atoms combine with each other to form H<sub>2</sub>. Therefore, CH<sub>4</sub> → CH<sub>3</sub>\* + H\* and H\* + H\* → H<sub>2</sub> are the most critical steps [48]. To explore the reasons for the effect of

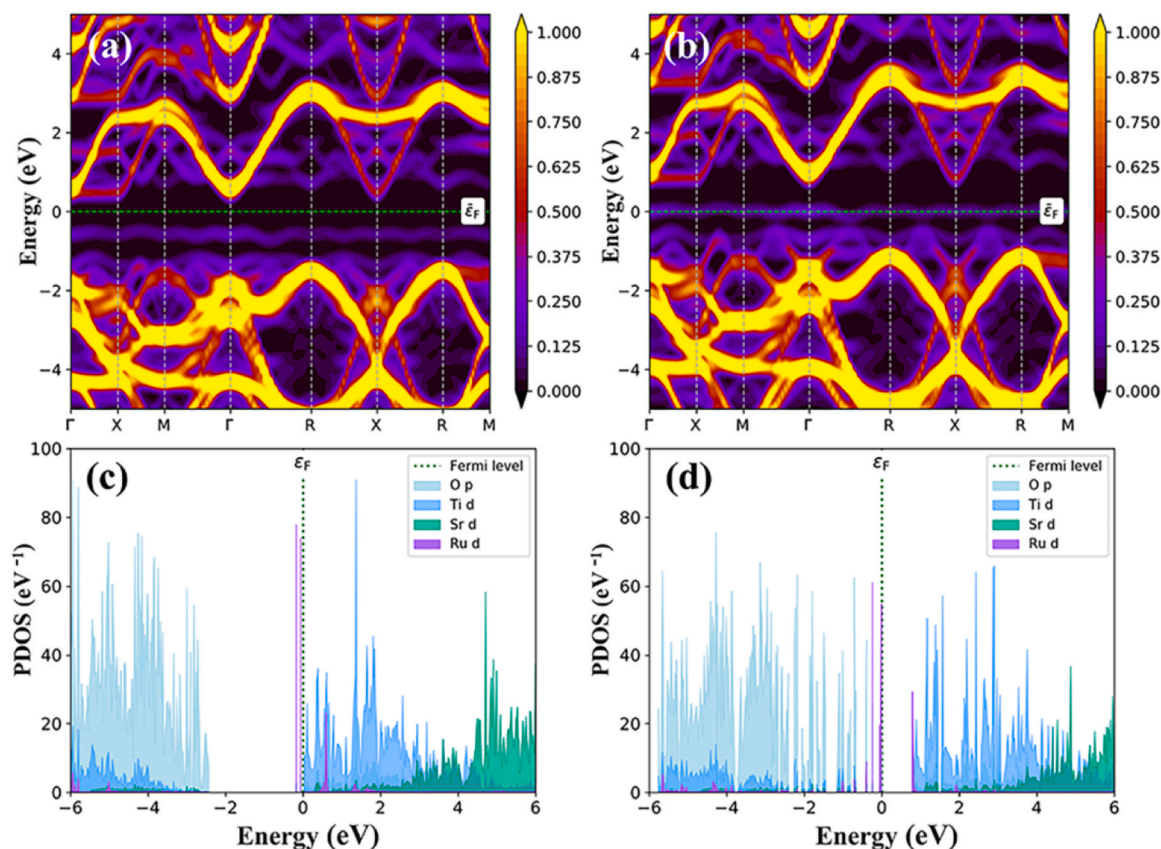


Fig. 5. (a, b) Effective energy band structures and (c, d) density of states of Ru/SrTiO<sub>3</sub> catalyst models in the absence and presence of light.

photogenerated charge on the DRM reaction performance, DFT calculations were performed for these key steps.

In this section, an oversized model closer to the real catalyst (it contains 122 atoms, including 22 Ru atoms) was built in order to calculate more reliable data. Fig. S6 shows the computed model. Four electrons were added to the entire Ru cluster and then performed charge difference density calculations on the model (Fig. S7). It was found that the charges are more likely to accumulate at the interface (pink indicates charge accumulation). This also indicates that the Ru atoms at the interface may be better active sites. Therefore, the adsorbed species are placed near the interface and their structure is optimized to achieve the minimum energy position. Fig. 6(a) and Table 2 show the structural details and reaction energy barriers of the adsorbed species.

As shown in Fig. 6(b), in the normal state, the activation energy required for the dissociation of CH<sub>4</sub> into CH<sub>3</sub>\* and H\* is 288.0 kJ/mol; however, in the electron-rich state, the activation energy required for the dissociation of CH<sub>4</sub> is 107.5 kJ/mol (a 180.5 kJ/mol decrease in activation energy); this implies that the electron-rich condition can promote the dissociation of CH<sub>4</sub> and generate more H\* to participate in the subsequent reaction.

Fig. 6(c) shows the H<sub>2</sub> production pathways in the normal state and the electron-rich state. The energy barrier of H<sub>2</sub> production in the normal state is 335.0 kJ/mol, whereas it decreases to 271.7 kJ/mol in the electron-rich state, indicating that the electron-rich state of Ru on the catalyst also contributes to the H<sub>2</sub> production. These results show that CH<sub>4</sub> sheds more H\* in the presence of light, and more H\* will participate in the subsequent reaction.

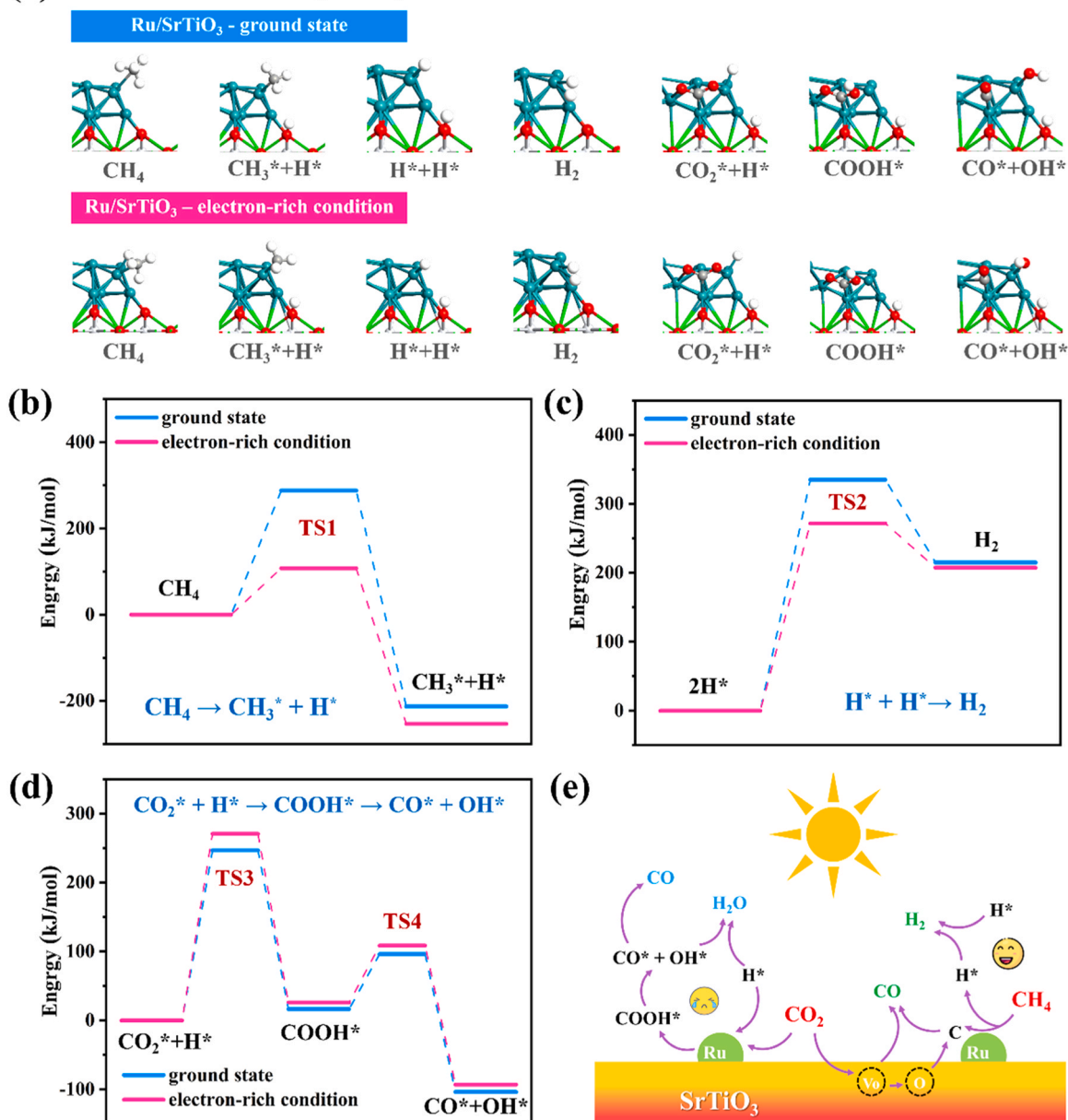
The RWGS reaction is the most important side reaction in DRM. The first step of the RWGS reaction involves CO<sub>2</sub> and H\*, which form COOH\* and then CO\* and OH\*. This process consumes H\*, generating H<sub>2</sub>O and more CO while reducing H<sub>2</sub> formation and lowering the H<sub>2</sub>/CO ratio [48]. Previous research on catalytic activity has demonstrated that

light is beneficial for enhancing the H<sub>2</sub>/CO ratio as well as for the RWGS reaction. To confirm this conclusion, DFT calculations were performed.

As shown in Fig. 6(d), in the step diagram of the RWGS reaction, the energy barriers in the electron-rich state are all higher than those in the normal state, which means that light is unfavorable for the formation of COOH\*, CO\* and OH\*. Therefore, it can be demonstrated that light is beneficial to reduce the RWGS reaction.

The combined DFT calculations showed that light promotes the dissociation of CH<sub>4</sub> and the H\* dissociated from CH<sub>4</sub> is more inclined to participate in the formation of H<sub>2</sub> rather than competing for RWGS reactions to form CO and H<sub>2</sub>O. Thus, the H<sub>2</sub>/CO ratio under photothermal conditions is consistently higher than those obtained for purely thermal reaction processes.

Based on the above discussion, we present insights into the DRM reaction mechanism on Ru/SrTiO<sub>3</sub> catalysts under photothermal and thermocatalytic reaction conditions, as shown in Fig. 6(e). The catalyst carrier is SrTiO<sub>3</sub>, and Ru elements are uniformly distributed on the surface of SrTiO<sub>3</sub>. During the DRM reaction, CH<sub>4</sub> is gradually dissociated upon the activation of the active metal Ru to produce a large amount of H\* and C. C reacts with lattice oxygen to produce CO [49], while H\* combines with each other to produce H<sub>2</sub>. On the one hand, CO<sub>2</sub> combines with oxygen vacancies to break the C=O bond and produce CO [34]; On the other hand, it participates in the inverse water-gas reaction process along with H\* on Ru, simultaneously consuming H\* and producing H<sub>2</sub>O and CO. Light irradiation on the catalyst surface induces electron transfer from the SrTiO<sub>3</sub> carrier to Ru. Meanwhile, the Schottky barrier formed between Ru and SrTiO<sub>3</sub> facilitates the separation of e<sup>-</sup> and h<sup>+</sup>, making it difficult for them to compound together. In this process, a large number of electrons accumulated by Ru maintains its reduced state to secure the number of active centers while also participating in the DRM reaction via interband transitions, which lower the activation energy barrier for CH<sub>4</sub> dissociation and H<sub>2</sub> generation and

**(a) DRM reaction critical pathways**

**Fig. 6.** Critical reaction pathways in the ground state with electron-rich conditions. (a) Atomic configuration (silver, green, red, blue, gray, and white spheres represent Ti, Sr, O, Ru, C, and H atoms, respectively), (b) methane cracking, (c) hydrogen generation, (d) inverse water–gas reaction, and (e) schematic diagram of the photothermal DRM reaction over the Ru/SrTiO<sub>3</sub> catalyst.

hinder the generation of COOH\*, CO\* and OH\*. Therefore, light significantly improves the catalytic capacity, stability, and H<sub>2</sub>/CO ratio of Ru/SrTiO<sub>3</sub> catalysts.

#### 4. Conclusion

Herein, Ru/SrTiO<sub>3</sub> catalysts were prepared using a hydrothermal method in which SrTiO<sub>3</sub> acted as a carrier for the DRM reaction. The results showed that the catalyst exhibited an enhanced catalytic ability, stability, and H<sub>2</sub>/CO ratio under photothermal conditions. The higher temperature generated by light and the light-induced charge transfer are the two reasons for the enhanced catalytic performance under light. And, the light-induced charge transfer plays a more critical role in the light-driven DRM. Based on in situ-irradiated XPS and DFT calculations, light can effectively induce charge transfer from SrTiO<sub>3</sub> to Ru, thereby maintaining the amount of Ru<sup>0</sup> to achieve enhanced catalyst stability

and participating in the DRM reaction via interband transitions. This can effectively reduce the reaction energy barrier for CH<sub>4</sub> dissociation and H<sub>2</sub> generation and enhance the catalytic activity while suppressing the RWGS reaction and improving the H<sub>2</sub>/CO ratio. Our study explores the role of light in the DRM reaction and deepens our understanding of the photothermal DRM reaction mechanism. Additionally, this study can provide useful theoretical guidance for the future solar photothermal conversion of greenhouse gases.

#### Funding Sources

Program of Science and Technology Innovation Team in Bingtuan (No.2020CB006).



**Table 2**

Activation energy of Ru/SrTiO<sub>3</sub> in DRM reaction under dark and light reaction conditions for the main reaction paths.

System	Reaction route	species	Elementary reactions	Transition State	Ea (kJ/mol)
Ru/SrTiO <sub>3</sub> -Dark	CH <sub>4</sub> cracking	CH <sub>4</sub>	CH <sub>4</sub> → CH <sub>3</sub> * + H*	TS1	288.0
	H <sub>2</sub> formation	H*	2 H* → H <sub>2</sub>	TS2	335.0
	RWGS	CO <sub>2</sub> * + H*	CO <sub>2</sub> * + H* → COOH*	TS3	246.7
		COOH*	COOH* → CO* + OH*	TS4	96.0
Ru/SrTiO <sub>3</sub> -Light	CH <sub>4</sub> cracking	CH <sub>4</sub>	CH <sub>4</sub> → CH <sub>3</sub> * + H*	TS1	107.5
	H <sub>2</sub> formation	H*	2 H* → H <sub>2</sub>	TS2	271.7
	RWGS	CO <sub>2</sub> * + H*	CO <sub>2</sub> * + H* → COOH*	TS3	270.7
		COOH*	COOH* → CO* + OH*	TS4	108.5

### CRedit authorship contribution statement

**Ying Tang:** Conceptualization, Data curation, Investigation, Theoretical simulation, Writing – original draft. **Yangyang Li:** Formal analysis, Resources, Methodology. **Wentao Bao:** Formal analysis, Resources. **Wenxia Yan:** Formal analysis, Methodology. **Jie Zhang:** Formal analysis, Visualization. **Yifan Huang:** Formal analysis, Visualization. **Han Li:** Formal analysis, Methodology. **Zijun Wang:** Writing – review & editing. **Minmin Liu:** Writing – review & editing. **Feng Yu:** Conceptualization, Funding acquisition, Investigation, Project administration, Supervision, Writing – review & editing.

### Declaration of Competing Interest

The authors declare that they have no known competing financial interests or personal relationships that could have appeared to influence the work reported in this paper.

### Data availability

Data will be made available on request.

### Acknowledgments

This work was financially supported by Program of Science and Technology Innovation Team in Bingtuan (No. 2020CB006).

### Appendix A. Supporting information

Supplementary data associated with this article can be found in the online version at doi:10.1016/j.apcatb.2023.123054.

### References

- [1] T.T.P. Pham, K.S. Ro, L. Chen, D. Mahajan, T.J. Siang, U.P.M. Ashik, J.-i Hayashi, D. Pham Minh, D.-V.N. Vo, Microwave-assisted dry reforming of methane for syngas production: a review, *Environ. Chem. Lett.* 18 (2020) 1987–2019.
- [2] D. Guo, Y. Lu, Y. Ruan, Y. Zhao, Y. Zhao, S. Wang, X. Ma, Effects of extrinsic defects originating from the interfacial reaction of CeO<sub>2-x</sub>-nickel silicate on catalytic performance in methane dry reforming, *Appl. Catal. B: Environ.* 277 (2020), 119278.
- [3] H. Liu, Y. Li, H. Wu, J. Liu, D. He, Effects of α- and γ-cyclodextrin-modified impregnation method on physicochemical properties of Ni/SBA-15 and its catalytic performance in CO<sub>2</sub> reforming of methane, *Chin. J. Catal.* 36 (2015) 283–289.
- [4] H. Liu, X. Meng, W. Yang, G. Zhao, D. He, J. Ye, Photo-thermal CO<sub>2</sub> reduction with methane on group VIII metals: In situ reduced WO<sub>3</sub> support for enhanced catalytic activity, *Chin. J. Catal.* 42 (2021) 1976–1982.
- [5] B. Abdullah, N.A. Abd Ghani, D.-V.N. Vo, Recent advances in dry reforming of methane over Ni-based catalysts, *J. Clean. Prod.* 162 (2017) 170–185.
- [6] H. Liu, X. Meng, T.D. Dao, H. Zhang, P. Li, K. Chang, T. Wang, M. Li, T. Nagao, J. Ye, Conversion of carbon dioxide by methane reforming under visible-light irradiation: surface-plasmon-mediated nonpolar molecule activation, *Angew. Chem. Int. Ed.* 54 (2015) 11545–11549.
- [7] J. Wang, R.-t Guo, Z.-x Bi, X. Chen, X. Hu, W.-g Pan, A review on TiO<sub>2-x</sub>-based materials for photocatalytic CO<sub>2</sub> reduction, *Nanoscale* 14 (2022) 11512–11528.
- [8] B. Han, W. Wei, L. Chang, P. Cheng, Y.H. Hu, Efficient visible light photocatalytic CO<sub>2</sub> reforming of CH<sub>4</sub>, *ACS Catal.* 6 (2016) 494–497.
- [9] J. Sun, D. Yamaguchi, L. Tang, S. Periasamy, H. Ma, J.N. Hart, K. Chiang, Enhancement of oxygen exchanging capability by loading a small amount of ruthenium over ceria-zirconia on dry reforming of methane, *Adv. Powder Technol.* 33 (2022), 103407.
- [10] J. Yang, J. Wang, J. Zhao, Y. Bai, H. Du, Q. Wang, B. Jiang, H. Li, CO<sub>2</sub> conversion via dry reforming of methane on a core-shell Ru@SiO<sub>2</sub> catalyst, *J. CO<sub>2</sub> Util.* 57 (2022), 101893.
- [11] L. He, Y. Ren, Y. Fu, B. Yue, S.C.E. Tsang, H. He, Morphology-dependent catalytic activity of Ru/CeO<sub>2</sub> in Dry Reforming of Methane, *Molecules* 24 (2019) 526.
- [12] M. Usman, W.M.A. Wan Daud, H.F. Abbas, Dry reforming of methane: Influence of process parameters—A review, *Renew. Sustain. Energy Rev.* 45 (2015) 710–744.
- [13] Y. Wang, L. Yao, Y. Wang, S. Wang, Q. Zhao, D. Mao, C. Hu, Low-temperature catalytic CO<sub>2</sub> dry reforming of methane on Ni-Si/ZrO<sub>2</sub> catalyst, *ACS Catal.* 8 (2018) 6495–6506.
- [14] X. Li, J. Yin, J. Zhang, Y. Wang, X. Song, Y. Zhang, X. Ren, Hydrogen embrittlement and failure mechanisms of multi-principal element alloys: A review, *J. Mater. Sci. Technol.* 122 (2022) 20–32.
- [15] F. Pan, X. Xiang, Z. Du, E. Sarnello, T. Li, Y. Li, Integrating photocatalysis and thermocatalysis to enable efficient CO<sub>2</sub> reforming of methane on Pt supported CeO<sub>2</sub> with Zn doping and atomic layer deposited MgO overcoating, *Appl. Catal. B: Environ.* 260 (2020), 118189.
- [16] Z. Rao, Y. Cao, Z. Huang, Z. Yin, W. Wan, M. Ma, Y. Wu, J. Wang, G. Yang, Y. Cui, Z. Gong, Y. Zhou, Insights into the nonthermal effects of light in dry reforming of methane to enhance the H<sub>2</sub>/CO ratio near unity over Ni/Ga<sub>2</sub>O<sub>3</sub>, *ACS Catal.* 11 (2021) 4730–4738.
- [17] Y. Yang, Z. Chai, X. Qin, Z. Zhang, A. Muhetaer, C. Wang, H. Huang, C. Yang, D. Ma, Q. Li, D. Xu, Light-induced redox looping of a rhodium/CeWO<sub>3</sub> photocatalyst for highly active and robust dry reforming of methane, *Angew. Chem. Int. Ed.* 61 (2022), e202200567.
- [18] Q. Zhang, M. Mao, Y. Li, Y. Yang, H. Huang, Z. Jiang, Q. Hu, S. Wu, X. Zhao, Novel photoactivation promoted light-driven CO<sub>2</sub> reduction by CH<sub>4</sub> on Ni/CeO<sub>2</sub> nanocomposite with high light-to-fuel efficiency and enhanced stability, *Appl. Catal. B: Environ.* 239 (2018) 555–564.
- [19] F. Pan, X. Xiang, W. Deng, H. Zhao, X. Feng, Y. Li, A. Novel, Photo-thermochemical approach for enhanced carbon dioxide reforming of methane, *ChemCatChem* 10 (2018) 940–945.
- [20] T. Xie, Z.-Y. Zhang, H.-Y. Zheng, K.-D. Xu, Z. Hu, Y. Lei, Enhanced photothermal catalytic performance of dry reforming of methane over Ni/mesoporous TiO<sub>2</sub> composite catalyst, *Chem. Eng. J.* 429 (2022), 132507.
- [21] Z. Du, F. Pan, E. Sarnello, X. Feng, Y. Gang, T. Li, Y. Li, Probing the origin of photocatalytic effects in photothermochemical dry reforming of methane on a Pt/CeO<sub>2</sub> catalyst, *J. Phys. Chem. C* 125 (2021) 18684–18692.
- [22] K. Takeda, A. Yamaguchi, Y. Cho, O. Anjaneyulu, T. Fujita, H. Abe, M. Miyauchi, Metal carbide as a light-harvesting and anticoking catalysis support for dry reforming of methane, *Glob. Chall.* 4 (2020) 1900067.
- [23] M. Mao, Q. Zhang, Y. Yang, Y. Li, H. Huang, Z. Jiang, Q. Hu, X. Zhao, Solar-light-driven CO<sub>2</sub> reduction by methane on Pt nanocrystals partially embedded in mesoporous CeO<sub>2</sub> nanorods with high light-to-fuel efficiency, *Green. Chem.* 20 (2018) 2857–2869.
- [24] D. Takami, Y. Ito, S. Kawaharasaki, A. Yamamoto, H. Yoshida, Low temperature dry reforming of methane over plasmonic Ni photocatalysts under visible light irradiation, *Sustain. Energy Fuels* 3 (2019) 2968–2971.
- [25] B. Tahir, M. Tahir, N.A.S. Amin, Silver loaded protonated graphitic carbon nitride (Ag/pg-C<sub>3</sub>N<sub>4</sub>) nanosheets for stimulating CO<sub>2</sub> reduction to fuels via photocatalytic bi-reforming of methane, *Appl. Surf. Sci.* 493 (2019) 18–31.
- [26] S. Wibowo, A. Yamaguchi, S. Shoji, T. Fujita, H. Abe, M. Miyauchi, Photo-assisted dry reforming of methane over strontium titanate, *Chem. Lett.* 47 (2018) 935–937.
- [27] C. Egawa, Methane dry reforming reaction on Ru(0 0 1) surfaces, *J. Catal.* 358 (2018) 35–42.
- [28] Z. Liu, F. Zhang, N. Rui, X. Li, L. Lin, L.E. Betancourt, D. Su, W. Xu, J. Cen, K. Attenkofer, H. Idriss, J.A. Rodriguez, S.D. Senanayake, Highly active ceria-supported Ru catalyst for the dry reforming of methane: in situ identification of Ru<sup>δ+</sup>-Ce<sup>3+</sup> interactions for enhanced conversion, *ACS Catal.* 9 (2019) 3349–3359.
- [29] X. Chen, X. Chen, S. Cai, J. Chen, W. Xu, H. Jia, J. Chen, Catalytic combustion of toluene over mesoporous Cr<sub>2</sub>O<sub>3</sub>-supported platinum catalysts prepared by in situ pyrolysis of MOFs, *Chem. Eng. J.* 334 (2018) 768–779.
- [30] A. Hadj Youssef, J. Zhang, A. Ehteshami, G. Kolhatkar, C. Dab, D. Berthomieu, A. Merlen, F. Légaré, A. Ruediger, Symmetry-forbidden-mode detection in SrTiO<sub>3</sub> nanoislands with tip-enhanced raman spectroscopy, *J. Phys. Chem. C* 125 (2021) 6200–6208.
- [31] H. Trabelsi, M. Bejar, E. Dhahri, M.P.F. Graça, M.A. Valente, M.J. Soares, N. A. Sobolev, Raman, EPR and ethanol sensing properties of oxygen-Vacancies SrTiO<sub>3-s</sub> compounds, *Appl. Surf. Sci.* 426 (2017) 386–390.
- [32] Y. Li, Z. Rao, Z. Liu, J. Zeng, W. Bao, Z. Wang, J. Li, F. Yu, B. Dai, Y. Zhou, Photo-assisted CO/CO<sub>2</sub> methanation over Ni/TiO<sub>2</sub> catalyst: experiment and density functional theory calculation, *ChemCatChem* 14 (2022), e202200182.

- [33] D. Luan, H. Jiang, Theoretical study of surface segregation and ordering in Ni-based bimetallic surface alloys, *J. Chem. Phys.* 154 (2021), 074702.
- [34] J. Lee, D.C. Sorescu, X. Deng, Electron-induced dissociation of CO<sub>2</sub> on TiO<sub>2</sub>(110), *J. Am. Chem. Soc.* 133 (2011) 10066–10069.
- [35] T.A. Le, J. Kim, J.K. Kang, E.D. Park, CO and CO<sub>2</sub> methanation over Ni/Al@Al<sub>2</sub>O<sub>3</sub> core-shell catalyst, *Catal. Today* 356 (2020) 622–630.
- [36] M. Zhang, J. Wang, H. Xue, J. Zhang, S. Peng, X. Han, Y. Deng, W. Hu, Acceptor-doping accelerated charge separation in Cu<sub>2</sub>O photocathode for photoelectrochemical water splitting: theoretical and experimental studies, *Angew. Chem. Int. Ed.* 59 (2020) 18463–18467.
- [37] S. Tonda, S. Kumar, M. Bhardwaj, P. Yadav, S. Ogale, g-C<sub>3</sub>N<sub>4</sub>/NiAl-LDH 2D/2D hybrid heterojunction for high-performance photocatalytic reduction of CO<sub>2</sub> into renewable fuels, *ACS Appl. Mater. Interfaces* 10 (2018) 2667–2678.
- [38] X. Zhang, L. Yu, C. Zhuang, T. Peng, R. Li, X. Li, Highly asymmetric phthalocyanine as a sensitizer of graphitic carbon nitride for extremely efficient photocatalytic H<sub>2</sub> production under near-infrared light, *ACS Catal.* 4 (2014) 162–170.
- [39] Q.-M. Sun, J.-J. Xu, F.-F. Tao, W. Ye, C. Zhou, J.-H. He, J.-M. Lu, Boosted inner surface charge transfer in perovskite nanodots@mesoporous titania frameworks for efficient and selective photocatalytic CO<sub>2</sub> reduction to methane, *Angew. Chem. Int. Ed.* 61 (2022), e202200872.
- [40] C. Han, B. Wang, N. Wu, S. Shen, Y. Wang, Deep and selective photoreduction of CO<sub>2</sub> to CH<sub>4</sub> over ultrafine Pt nanoparticles-decorated SiC nanosheets, *Appl. Surf. Sci.* 515 (2020), 145952.
- [41] H. Liu, T.D. Dao, L. Liu, X. Meng, T. Nagao, J. Ye, Light assisted CO<sub>2</sub> reduction with methane over group VIII metals: Universality of metal localized surface plasmon resonance in reactant activation, *Appl. Catal. B: Environ.* 209 (2017) 183–189.
- [42] J. Zhang, C. Peng, H. Wang, P. Hu, Identifying the role of photogenerated holes in photocatalytic methanol dissociation on rutile TiO<sub>2</sub>(110), *ACS Catal.* 7 (2017) 2374–2380.
- [43] S. Wei, F. Wang, M. Dan, S. Yu, Y. Zhou, Vanadium (V) and Niobium (Nb) as the most promising co-catalysts for hydrogen sulfide splitting screened out from 3d and 4d transition metal single atoms, *Int. J. Hydrog. Energy* 45 (2020) 17480–17492.
- [44] H.-Y.T. Chen, S. Tosoni, G. Pacchioni, Adsorption of ruthenium atoms and clusters on anatase TiO<sub>2</sub> and tetragonal ZrO<sub>2</sub>(101) surfaces: a comparative DFT study, *J. Phys. Chem. C* 119 (2015) 10856–10868.
- [45] Z. Liu, F. Yu, D. Dong, R. Gui, W. Li, R. Sun, Y. Wan, J. Dan, Q. Wang, B. Dai, Transition-metal-doped ceria carried on two-dimensional vermiculite for selective catalytic reduction of NO with CO: Experiments and density functional theory, *Appl. Surf. Sci.* 566 (2021), 150704.
- [46] Y. Li, Z. Liu, Z. Rao, F. Yu, W. Bao, Y. Tang, H. Zhao, J. Zhang, Z. Wang, J. Li, Z. Huang, Y. Zhou, Y. Li, B. Dai, Experimental and theoretical insights into an enhanced CO<sub>2</sub> methanation mechanism over a Ru-based catalyst, *Appl. Catal. B: Environ.* 319 (2022), 121903.
- [47] Z. Liu, D.C. Grinter, P.G. Lustemberg, T.-D. Nguyen-Phan, Y. Zhou, S. Luo, I. Waluyo, E.J. Crumlin, D.J. Stacchiola, J. Zhou, J. Carrasco, H.F. Busnengo, M. V. Ganduglia-Pirovano, S.D. Senanayake, J.A. Rodriguez, Dry Reforming of methane on a highly-active Ni-CeO<sub>2</sub> catalyst: effects of metal-support interactions on C–H bond breaking, *Angew. Chem. Int. Ed.* 55 (2016) 7455–7459.
- [48] L. Foppa, M.-C. Silaghi, K. Larmier, A. Comas-Vives, Intrinsic reactivity of Ni, Pd and Pt surfaces in dry reforming and competitive reactions: Insights from first principles calculations and microkinetic modeling simulations, *J. Catal.* 343 (2016) 196–207.
- [49] W.-J. Jang, J.-O. Shim, H.-M. Kim, S.-Y. Yoo, H.-S. Roh, A review on dry reforming of methane in aspect of catalytic properties, *Catal. Today* 324 (2019) 15–26.